KeAi
CHINESE ROOTS
GLOBAL IMPACT

Contents lists available at ScienceDirect

Advanced Powder Materials

journal homepage: www.keaipublishing.com/en/journals/advanced-powder-materials



Long- and short-range orders in 10-component compositionally complex ceramics



Dawei Zhang ^{a,b}, Yan Chen ^b, Heidy Vega ^c, Tianshi Feng ^d, Dunji Yu ^b, Michelle Everett ^b, Joerg Neuefeind ^b, Ke An ^b, Renkun Chen ^{a,d}, Jian Luo ^{a,f,*}

- ^a Program of Materials Science and Engineering, University of California San Diego, La Jolla 92093, USA
- ^b Neutron Scattering Division, Oak Ridge National Laboratory, Oak Ridge 38731, USA
- ^c Department of Biochemistry and Chemistry, University of California San Diego, La Jolla 92093, USA
- ^d Department of Mechanical & Aerospace Engineering, University of California San Diego, La Jolla 92093, USA
- f Department of NanoEngineering, University of California San Diego, La Jolla 92093, USA

ARTICLE INFO

Keywords: Neutron diffraction

Neutron total scattering Order-disorder transition Short-range order High-entropy ceramics Compositionally complex ceramics

ABSTRACT

Neutron diffraction and total scattering are combined to investigate a series of single-phase 10-component $compositionally \ \ complex \ \ fluorite-based \ \ oxides, \ \ [(Pr_{0.375}Nd_{0.375}Yb_{0.25})_2(Ti_{0.5}Hf_{0.25}Zr_{0.25})_2O_7]_{1-x}[(DyHoErNb)]_{1} + (DyHoErNb)_{1} + (DyHoErNb)_{1} + (DyHoErNb)_{2} + (DyHoErNb)$ O₇]_x, denoted as 10CCFBO_{xNb}. A long-range order-disorder transition (ODT) occurs at x ½ 0.81 0.01 from the ordered pyrochlore to disordered defect fluorite. In contrast to ternary oxides, this ODT occurs abruptly without an observable two-phase region; moreover, the phase stability in 10CCFBOs deviates from the well-established criteria for simpler oxides. Rietveld refinements of neutron diffraction patterns suggest that this ODT occurs via the migration of oxygen anions from the position 48f to 8a, with a small final jump at the ODT; however, the 8a oxygen occupancy changes gradually (without an observable discontinuous jump). We further discover diffuse scattering in Nb-rich compositions, which suggests the presence of short-range order. Using small-box modelling, four compositions near ODT (x % 0.75, 0.8, 0.85, and 1) can be better fitted by C2221 weberite ordering for the local polyhedral structure at nanoscale. Interestingly, 10CCFBO_{0.75Nb} and 10CCFBO_{0.8Nb} possess both long-range pyrochlore order and short-range weberite-type order, which can be understood from severe local distortion of the pyrochlore polyhedral structure. Thus, weberite-type short-range order emerges before the ODT, coexisting and interacting with long-range pyrochlore order. After the ODT, the long-range pyrochlore order vanishes but the short-range weberite-type order persists in the long-range disordered defect fluorite structure. Notably, a drop in the thermal conductivity coincides with emergence of the short-range order, instead of the long-range ODT.

1. Introduction

Fluorite-based oxides are a fascinating class of functional and structural ceramics with applications in solid oxide fuel cells (SOFCs) [1,2] and thermal barrier coatings (TBCs) [3–5], amongst other areas. They exhibit versatile compositional space and structural diversity. Here, the cubic fluorite (AO₂₋₆), as well as the disordered defect fluorite (A₄O₇), is the basis structure. The cubic pyrochlore (A₂B₂O₇) and orthorhombic weberite-type (A₃BO₇) structures represent two common derivative superstructures (of 2 2 2 and 2 2 2, respectively) with ordered cations and oxygen vacancies [6]. The phase transformations between these structures further enable tailoring of thermal, mechanical,

and other physical properties, including the radiation resistance [7,8]. Researchers have investigated the order-disorder transition (ODT) in fluorite-based oxides using X-ray diffraction [9,10], Raman spectroscopy [11], transmission electron microscopy [12,13], X-ray absorption near edge spectroscopy (XANES) [14], and neutron total scattering [15,16]. The investigation can be conducted at different length scales to probe both long- and short-range orders. Researchers discovered that the oxygen anion displacement from 48f to 8a is the major cause of the long-range fluorite-to-pyrochlore ODT in 2- or 3-component oxides [9, 16,17]. In addition, weberite-type short-range ordering has been reported in long-range-disordered defect fluorite structure [6,18,19]. For example, Drey et al. proposed that oxygen anion migration can create

https://doi.org/10.1016/j.apmate.2022.100098

Received 16 September 2022; Received in revised form 28 October 2022; Accepted 31 October 2022 Available online 4 November 2022

2772-834X/© 2022 Central South University. Publishing services by Elsevier B.V. on behalf of KeAi Communications Co. Ltd. This is an open access article under the CC BY license (http://creativecommons.org/licenses/by/4.0/).

^{*} Corresponding author. Department of NanoEngineering, Program of Materials Science and Engineering, University of California, San Diego, Office: Structural and Materials Engineering Building, Room 244G, 9500 Gilman Drive, Mail Code 0448, La Jolla 92093, USA.

E-mail addresses: jluo@alum.mit.edu, jluo@ucsd.edu (J. Luo).

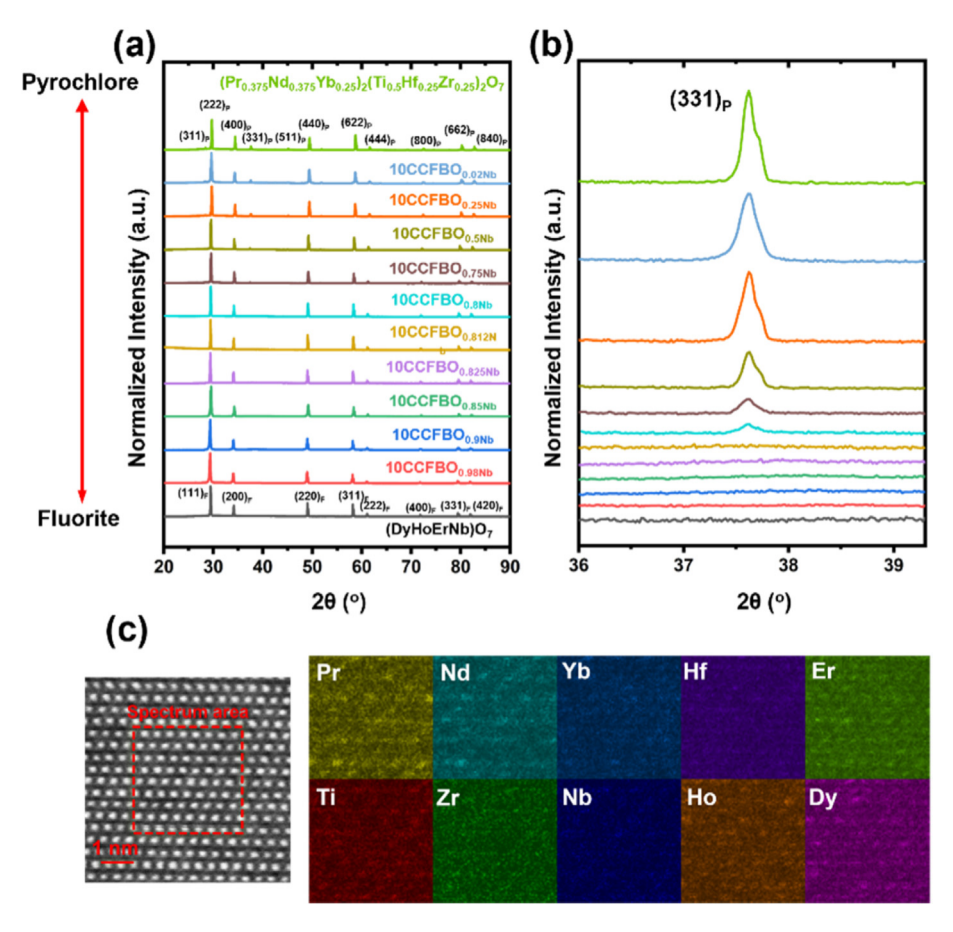


Fig. 1. (a) XRD spectra of the 10CCFBO_{xNb} series with pyrochlore and fluorite peaks indexed. (b) The enlarged pyrochlore superstructure (331)_p peak area (36-39). The long-range order-disorder transition (ODT) takes place between 10CCFBO_{0.8Nb} (cyan) and 10CCFBO_{0.812Nb} (dark yellow). Note that the small side peaks on the left of the (331)_p peaks were resulted from Cu Ka1 and Ka2 radiation doublets. (c) STEM HAADF image of the pyrochlore 10CCFBO_{0.5Nb} taken along the [110] zone axis and corresponding EDS elemental maps of the area indicated by the dashed red square in the STEM HAADF image. Bright spots in elemental maps mostly correspond to atomic columns. Since the TEM specimen thickness is > 20 nm, compositional clustering (e.g., chemical shortrange ordering) at ~1 nm scale cannot be measured by STEM EDS mapping. Thus, variations in the intensities of the bright spots in the EDS elemental maps are likely due to measurement noises or statistical fluctuations at the atomic scale (because there is only a limited number of atoms of a given element in an atomic column, particularly in a 10-component system). Additional STEM EDS mapping at a lower magnification shown in Suppl. Fig. S2 demonstrates compositional homogeneity at ~20-100 nm scale.

seven-coordinated Zr sites to form weberite-type short-range ordering in ${\rm Ho_2(Ti_{2-y}Zr_y)O_7}$ [20]. These authors suggested that the formation of weberite-type nanodomains of different orientation can trigger the long-range disordering to form defect fluorite. In general, how the long-and short-range ordering vs. disordering form, interact, and affect various physical properties represents open scientific questions. In a fundamental and broader perspective, elucidating and controlling ordering vs. disordering at different length scales can open a window to tailor various physical properties.

In the last a few years, high-entropy ceramics (HECs), which possess high configurational entropy and compositional disorder, attracted great research interest. Many studies have been conducted to fabricate and characterize high-entropy rock-salt [21], perovskite [22,23], fluorite [24-29] (including defect fluorite [25-27]), pyrochlore [29-32], weberite [32], fergusonite [32], spinel [33] oxides, as well as high-entropy (MB₂, MB, M₃B₄, MB₄ and MB₆) borides [34-38], carbides [39-41], (MSi₂ and M₅Si₃) silicides [42,43], nitrides [44,45], and fluorides [46], amongst others [47,48]. In particular, high-entropy fluorite-based oxides have been reported for potential applications as thermal barrier coatings (TBCs) due to their low and reduced thermal conductivity and proper mechanical properties (e.g., moderate Young's moduli) [24-32]. Furthermore, it was proposed to broaden HECs to compositionally complex ceramics (CCCs) to include non-equimolar compositional designs and/or long- and short-range ordering, which reduce the configurational entropy, but provide additional dimensions to tailor or improve physical properties [32,47,49,50]. The vast majority of prior studies focused on equimolar five-component (occasionally four- or six-component) HECs [47,48]. Three recent studies further explored many-component (i.e., 10- to 21-component) non-equimolar CCCs (including ultrahigh-entropy compositions with long-range ordering) [32,51,52]. Here, long-range pyrochlore-to-fluorite [51,52] and pyrochlore-to-weberite [32] phase transformations (including a

redox-induced ODT [52]) have been reported. However, the atomic level phase transformation and ordering/disordering mechanisms in these many-component CCCs have not yet been investigated.

Thanks to their sensitivity, neutron diffraction and total scattering can provide high-quality data to characterize both long- and short-range orders. In 2020, Jiang et al. reported a study to combine neutron diffraction and total scattering to analyze high-entropy pyrochlore oxides [53]. In 2022, Wright et al. reported a neutron total scattering study to characterize the short-range ordering in five high-entropy rare earth niobates and tantalates (all in the long-range disordered defect fluorite structure) [25]. Both studies investigated 4- to 6-component equimolar or near-equimolar compositions, and they did not observe (therefore did not investigate) any ODT. Thus, the atomic level mechanisms of the compositionally induced ODT in HECs and CCCs, as well as the interaction and competition of short- and long-range ordering vs. disordering, have not yet been characterized by neutron diffraction or total scattering. These open scientific questions, which become more interesting and intriguing in many-component CCCs with high (or ultrahigh) configurational entropy and compositional disorder, motivated this study.

Herein, we designed a series of 10-component compositionally complex fluorite-based oxides with the following formula: $[(Pr_{0.375}Nd_{0.375}Yb_{0.25})_2(Ti_{0.5}Hf_{0.25}Zr_{0.25})_2O_7]_{1\text{-x}}[(DyHoErNb)O_7]_x,$ denoted as " 10CCFBO_{xNb} " for brevity, where x represents the fraction of Nb or niobate in the formula. This series of 10CCFBO_{xNb} composites all possesses single phase as confirmed by multi-scale characterization, with a long-range pyrochlore to defect fluorite ODT occurring at $x \sim 0.81$ 0.01. In addition, weberite-type short-range ordering was found for x > 00.5, interacting and competing with the long-range ODT. The weberitetype short-range ordering and pyrochlore long-range ordering and their interplay in 10CCFBOxNb, along with how the ODT takes place at the atomic scale, were revealed by combining the state-of-the-art neutron diffraction and neutron total scattering, along with Rietveld refinements

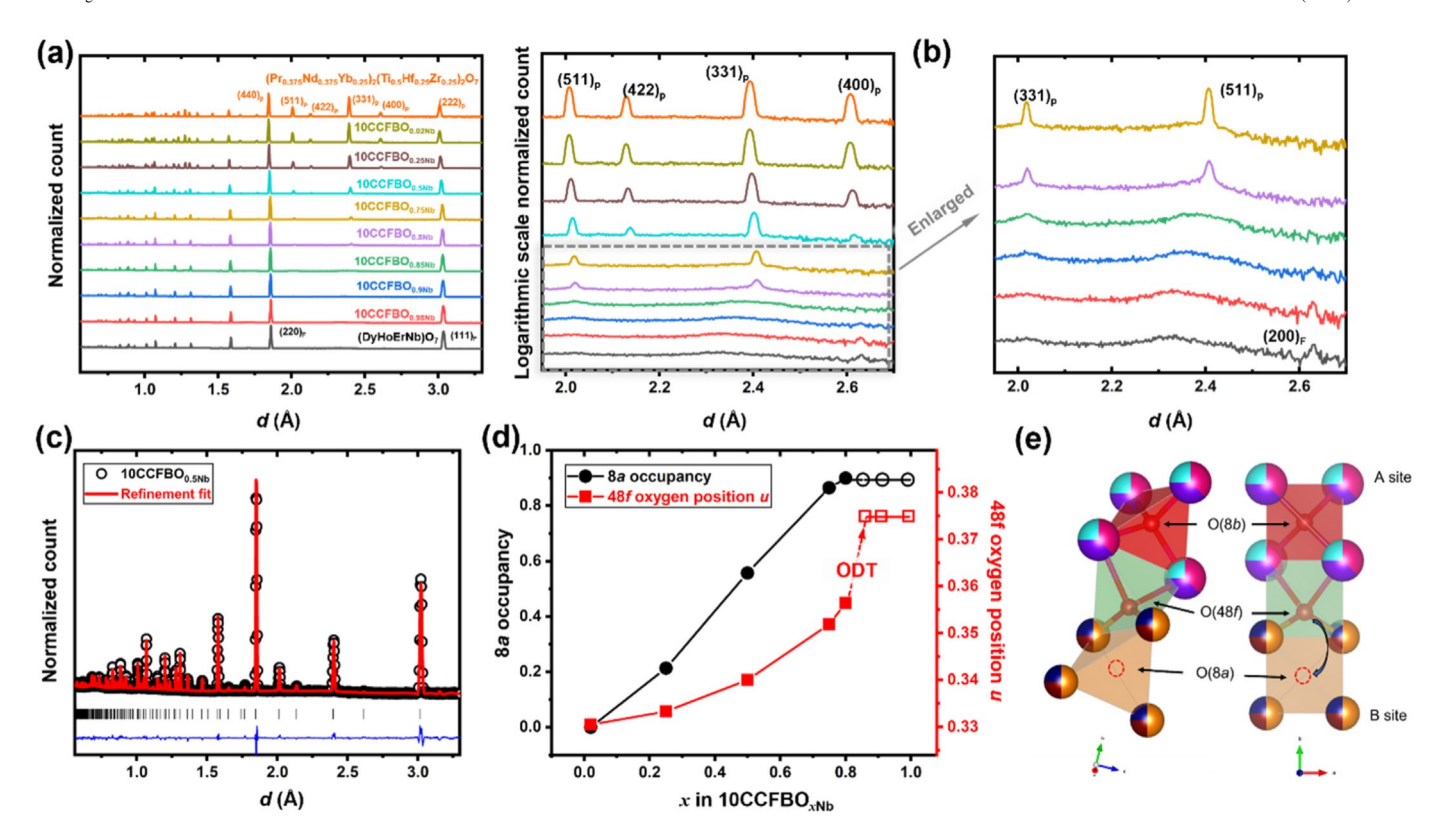


Fig. 2. (a) Neutron diffraction patterns of the $10\text{CCFBO}_{\text{xNb}}$ series of specimens. (b) Enlarged area showing the (331) pyrochlore superstructure peaks. The long-range pyrochlore to fluorite transition (ODT) happens in between $10\text{CCFBO}_{0.8\text{Nb}}$ and $10\text{CCFBO}_{0.85\text{Nb}}$. Broad background peaks appear for $10\text{CCFBO}_{\text{xNb}}$ specimens with high Nb contents (for x ½ 0.75, 0.8, 0.85, 0.9, and 1), which are attributed to the presence of short-range weberite-type orders based on a subsequent analysis. (c) A measured neutron diffraction pattern of $10\text{CCFBO}_{0.5\text{Nb}}$ (black circles) and the best Rietveld refinement fit with the Fd $\overline{3}$ m space group (red line). The blue line underneath represents the difference between experiment data and the refinement fit. The data fit for $10\text{CCFBO}_{0.5\text{Nb}}$ with Fd $\overline{3}$ m yields R_w ½ 0.031, which indicates a good fit. The short black lines under experimental data show the peaks index for the Fd $\overline{3}$ m structure. (d) Positional parameter u for 48f oxygen at the (u 1/8 1/8) and equivalent positions in the pyrochlore unit cell and occupancy of oxygen vacancy at position 8a (1/8 1/8 1/8) with increasing x in $10\text{CCFBO}_{\text{xNb}}$. The dense symbols stand for the pyrochlore compositions, and the hollow ones illustrate the corresponding 8a occupancy and u in defect fluorite composition. The oxygen anion has an abrupt movement close to the ODT, indicated by the dash line. (e) Schematic illustration of oxygen position and migration from 48f to 8a with increasing x.

and small-box modelling of pair distribution functions (PDFs). In addition to uncovering the atomic level ODT mechanism and the competition of long- and short-range ordering vs. disordering, we observed unusual phase stability in the $10\text{CCFBO}_{\text{NNb}}$ (in contrast to well-established criteria for ternary oxides) and the correlation of thermal conductivity with the emergent of short-range ordering instead of the long-range ODT.

2. Experimental procedure

2.1. Synthesis and fabrication of materials

All oxide precursors were purchased from US Research Nanomaterials Inc (Houston, TX). Powder precursors of the pyrochlore endmember $(Pr_{0.375}Nd_{0.375}Yb_{0.25})_2(Ti_{0.5}Hf_{0.25}Zr_{0.25})_2O_7 \quad \text{ and } \ \, \text{fluorite} \ \, \text{endmember}$ (DyHoErNb)O7 were first prepared separately. For each endmember, binary oxides were weighted, put in Y2O3-stablized ZrO2 jars with 10 mL isopropanol, and planetary ball milled for 24 h (using a PQN04 planetary miller, Across International) in parallel. After drying the powder at 75 C overnight, we mixed the powder of two endmembers with appropriate molar ratios to fabricate a series of twelve 10CCFBO_{xNb} imens for x ¼ 0, 0.02, 0.25, 0.5, 0.75, 0.8, 0.812, 0.825, 0.85, 0.9, 0.98 and 1, respectively. The nominal compositions are based on the weights of oxide precursors used in the synthesis, which are consistent with energy dispersive X-ray spectroscopy (EDS) measurements of the synthesized specimens within the typical EDS quantitative errors. The mixtures were placed in poly(methyl methacrylate) vials with tungsten carbide

inserts and balls for high-energy ball milling for 100 min (875 cycles/min using a SPEX 8000D miller, SPEX SamplePrep, USA). Finally, the powder was uniaxially pressed into 13 mm diameter pellets and placed on a Pt foil covered $\rm Al_2O_3$ crucibles for sintering. The Pt foil prevented the reaction between green body pellets and crucibles. The pellets were sintered at 1600 C in air for 24 h and furnace cooled to room temperature. The sintered pellets were grinded and polished for characterization.

2.2. Characterization

2.2.1. Phase identification and compositional analysis

Synthesized specimens were characterized by X-ray diffraction (XRD, Miniflex II diffractometer, Rigaku, Japan) to probe the crystal structure. XRD was operated at 30 kV and 15 mA to collect the spectra with 0.02 step size and 2 s dwell time. Rietveld refinements of XRD were conducted using GSAS II to confirm the crystal structure and measure the lattice parameters and theoretical density.

Scanning electron microscopy (SEM, FEI Apero) was applied to examine the microstructure and elemental homogeneity of all specimens. Specimens for SEM characterization were hot mounted in acrylic and polished [51]. Elemental maps were generated using energy dispersive X-ray spectroscopy (EDS, Oxford N-MAX) to examine the compositional homogeneity with a 20 kV and 3.2 nA electron beam.

Scanning transmission electron microscopy (STEM) specimens were prepared by a dual-beam focused ion beam (FIB, FEI Scios Dualbeam). The STEM images and EDS analysis were obtained using a 300 kV, double aberration-corrected STEM (JEOL JEM-ARM300CF, Japan) with a high-

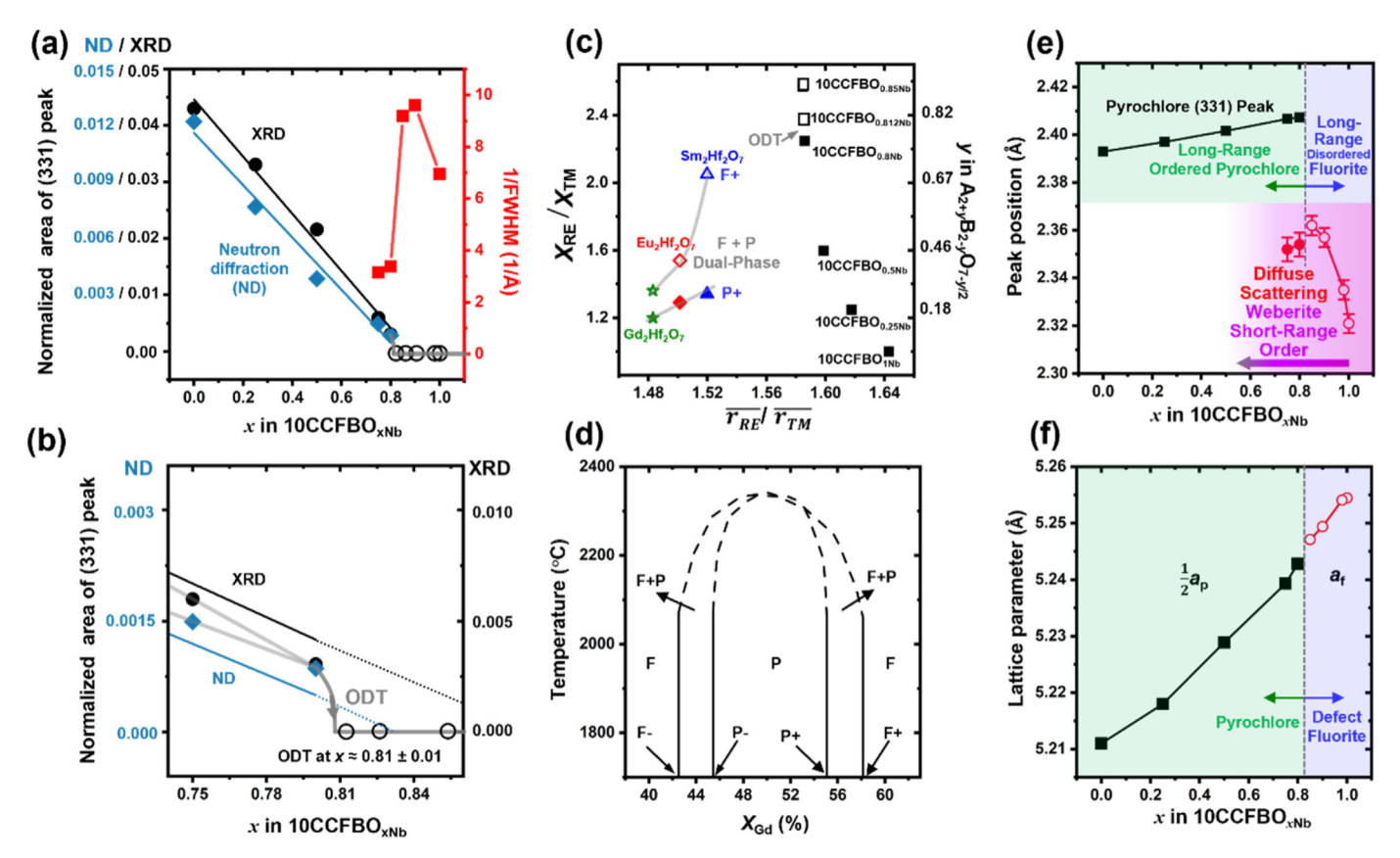


Fig. 3. (a) Normalized area of the (331) peak vs. x curves for the 10CCFBO_{xNb} series and linear least square fittings. The normalized peak areas were calculated based on the neutron diffraction (ND) patterns (indicated by the diamond symbols) and XRD (circle symbols). The left y axis was labeled with two scales for the data points calculated based on neutron/X-ray patterns. Reciprocal Full Width Half Maximum (1/FWHM) was determined from fitting the broad diffuse scattering peaks in neutron diffraction. The extrapolated x value for the vanishing of superstructure peaks from the best linear fittings are 0.82 0.02 for neutron diffraction and 0.87 0.03 for XRD, respectively. (b) Enlarged region near ODT. This analysis suggests an abrupt (331)_p vanishment of the (331) superstructure peak during the ODT occurring at x ~ 0.81 (accelerated from the linear extrapolated values, suggesting a final discontinuous jump). (c) The position of the (331)_p (represented by square symbols) and the diffuse scattering in long-range pyrochlore (dense circles for x 1/2 0.75 and 0.8) and defect fluorite (hollow circles for x 1/2 0.85, 0.9, 0.98, and 1) vs. x curves in the 10CCFBO_{xNb} series. (d) Lattice parameter vs. x in the 10CCFBO_{xNb} series. The pyrochlore lattice parameters (square symbols) are divided by two to correlate with those of the defect fluorite structure (circle symbols). All results here are based on neutron diffraction patterns obtained at the Vulcan diffractometer. (e) Plot of averaged cation radii ratio (r_{RE}/r_{TM}) and molar ratio (X_{RE}/X_{TM}) for the 10CCFBO_{xNb} series, where a rather abrupt ODT occurs between x ½ 0.8 and x ½ 0.812. For references, the r_{RE}/ r_{TM} vs. molar ratio (X_{RE}/X_{TM}) for the pyrochlore-fluorite dual-phase equilibria (phase boundaries) for three ternary RE₂Hf₂O₇ oxides are also plotted based on phase diagrams [ACerS-NIST database: Gd₂Hf₂O₇ (No. 9299), Eu₂Hf₂O₇ (No. 11158) and Sm₂Hf₂O₇ (No. 9333)], where the dual-phase compositional region increases with increasing r_{RE} / r_{TM} ratio. (f) The replotted phase diagram of Gd₂Hf₂O₇ (No.9299) to illustrate the dual-phase regions. The solid and hollow icons for the ternary hafnates in Panel (a) stand for the equilibrium compositions of pyrochlore (denoted as Pb) and fluorite phase (denoted as Fb) for the A/B > 1 or X_{Gd} > 0.5 side of the tie-line of the dual-phase region. Unlike ternary RE₂Hf₂O₇ oxides, the ODT in the 10CCFBO_{xNb} series takes place almost abruptly without an observable dual-phase region, despite it has a higher averaged cation radii ratio r_{RE}/r_{TM}.

angle annual dark field (HAADF) detector.

2.2.2. Neutron diffraction and Rietveld refinements

Neutron diffraction data were collected at the VULCAN diffractometer, at the Spallation Neutron Source (SNS), at the Oak Ridge National Laboratory (ORNL) [54]. Ten $10\text{CCFBO}_{\text{NNb}}$ samples were sintered pellets with 10 mm in diameter and 2.5 mm in thickness. The diffraction experiments were carried out at 290 K. All data shown in this paper used diffraction data from detector Bank 2 by optimizing the neutron path to reduce the neutron absorption.

The Rietveld refinements of all diffraction patterns were done with GSAS software. The refined parameters included the histogram scale factor, lattice parameter, isotropic atomic displacement parameters for A and B site metal cations and all oxygen positions (U_a , U_b , $U_{O(48f)}$, $U_{O(8b)}$, $U_{O(8a)}$), 36 coefficients of Chebyshev polynomial background, 2 coefficients describing Gaussian contributions to the Bragg peak shapes and finally the absorption factor due to elements like Dy. The pyrochlore structure does not have much flexibility for a cation position change and the only positional parameter allowed to be refined is the position u of

O(48f) at (u, 1/8, 1/8); noting that we adopt "u" here for the positional variable since "x" is used to denote the composition. The occupancy of three oxygen sites were also refined while maintaining the site balance: 48 O(48f) | | 8 O(8b) | | 8 O(8a) | 3 6 O sites per unit cell.

2.2.3. Neutron total scattering and pair distribution function

Pair distribution function (PDF) G(r) were obtained via neutron total scattering at Nanoscale-Ordered Materials Diffractometer (NOMAD BL-1B) at the SNS, ORNL. For $10\text{CCFBO}_{\text{NNb}}$ powder specimens (x %~0.75, 0.8, 0.85, and 1) were loaded into a 2.8 mm ID, 3 mm OD quartz capillary to a height of 30 cm with around 0.6 g total mass. The total scattering experiments were carried out at 290 K for a total accelerator proton charge of 8C, corresponding to about 92 min acquisition time at the full power. To produce the total scattering function S(Q), the background was subtracted for the data from six defector banks and the data were normalized to the intensity of vanadium. This function was Fourier-transformed with a sliding Q_{max} to obtain the neutron weighted pair distribution functions, GrP~%~r/2grP~1. The shortest distance

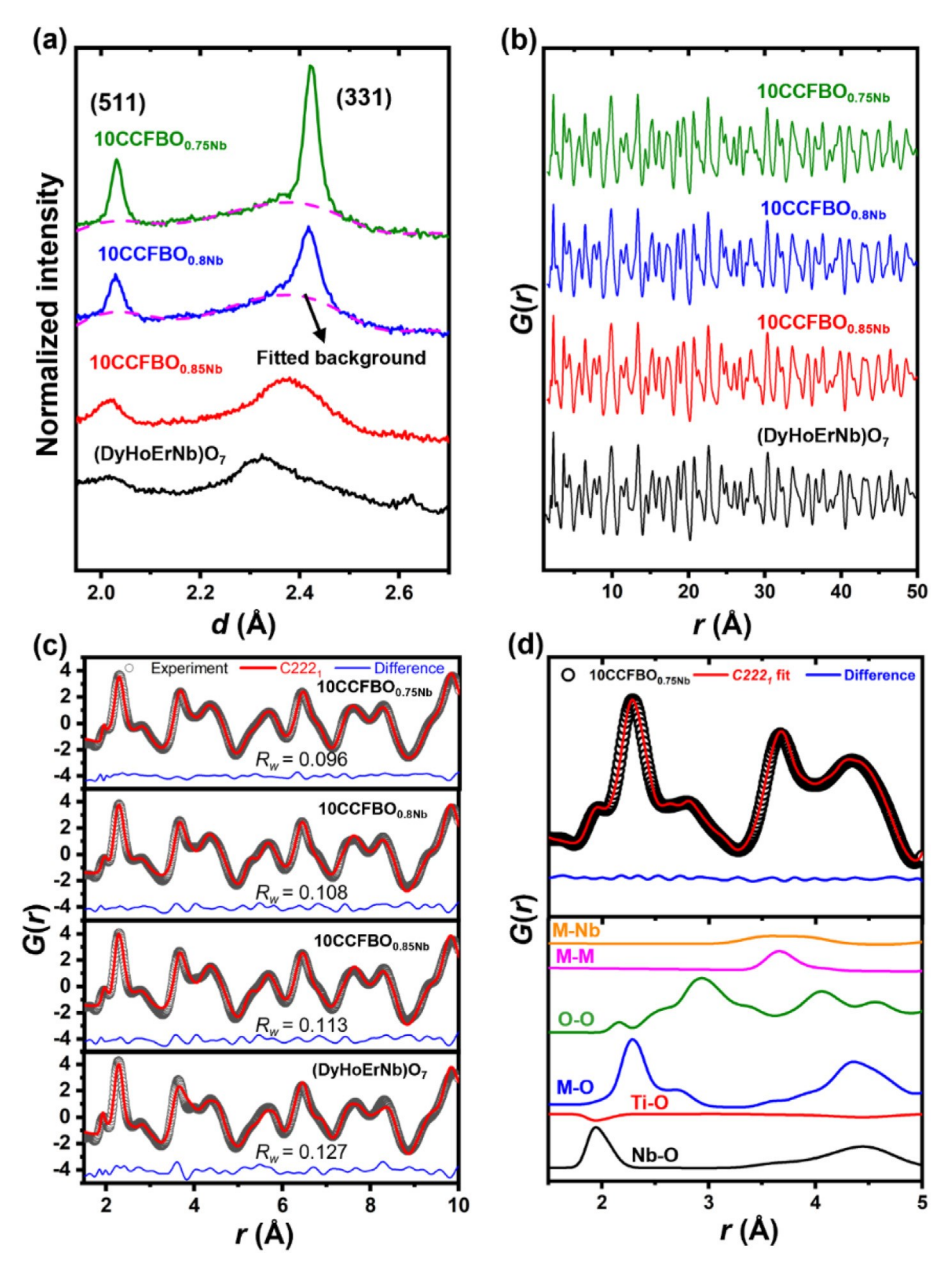


Fig. 4. (a) Neutron total scattering patterns with background fitting near the (331) peak from NOMAD (for better probing short-range ordering) and (b) neutron pair distribution functions (PDF) of the compositions near the ODT. (c) Small-box modelling of four selected 10CCFBO_{xNb} (x ¼ 0.75, 0.8, 0.85, and 1) with weberite-type C222₁ structures. (d) Partial PDFs of 10CCFBO_{0.75Nb} modeled based on the weberite C222₁ structure. Here, M stands for Pr. Nd. Dv. Ho. Er. Zr, and Hf. Black circles are the experimental data and red lines represent the model fittings. The partial PDFs for Nb-O and Ti-O show opposite trends in neutron scattering at the same position. The peak around 1.95 A gradually vanishes with decreasing x in 10CCFBOxNb because of the decreasing Nb content and increasing Ti content.

correlations were transformed with a Q_{max} ¼ 31:4 A^{1} . The momentum transfer, Q, is given as Q ¼ $\frac{4\pi \sin \theta}{\lambda}$, where θ and λ are the scattering angle and the neutron wavelength, respectively.

The analysis of PDF data was done with small-box modelling by the PDFgui software. Three different structures used to model the data were pyrochlore (Fd $\overline{3}$ m), defect fluorite (Fm $\overline{3}$ m), and weberite-type (C222₁) structures. The refined parameters for the pyrochlore, defect fluorite, and weberite-type structures are listed in the Supplementary Method section (in Supplementary Material). We note that there are more degrees of freedom for cation and anion displacements for the weberite-type (C222₁) structure. Hence, 27 parameters were refined for the space group C222₁. Multiple elements occupying A or B site were refined with the same XYZ position and ADP.

2.3. Thermal conductivity measurements

The thermal diffusivity was measured using a Laser Flash Analyzer (LFA 467 HT HyperFlash, NETZSCH, Germany). All measurements were conducted from room temperature (25 C) up to $600 \, \text{C}$ in an Ar gas

environment, with five individual measurements at each temperature point. Thermal conductivity was determined from thermal diffusivity (α), density (ρ), and specific heat (c_{ρ}) with the following equation:

$$k_{measured} \% \alpha \rho c_p$$
 (1)

The thermal conductivity was further corrected for porosity based on the following equation [55]:

$$k \, \frac{1}{\sqrt[6]{1} \, Pb^{3-2}}$$
 (2)

3. Results and discussion

3.1. Single-phase formation in 10-component oxides

All XRD patterns of the 10CCFBO_{xNb} specimens exhibit either single-phase defect fluorite A₄O₇ (Fm $\overline{3}$ m) or single-phase pyrochlore A₂B₂O₇ (Fd $\overline{3}$ m) structure (Fig. 1a), which can be differentiated by the (331)_p superstructure peak due to the cation and oxygen anion ordering in the

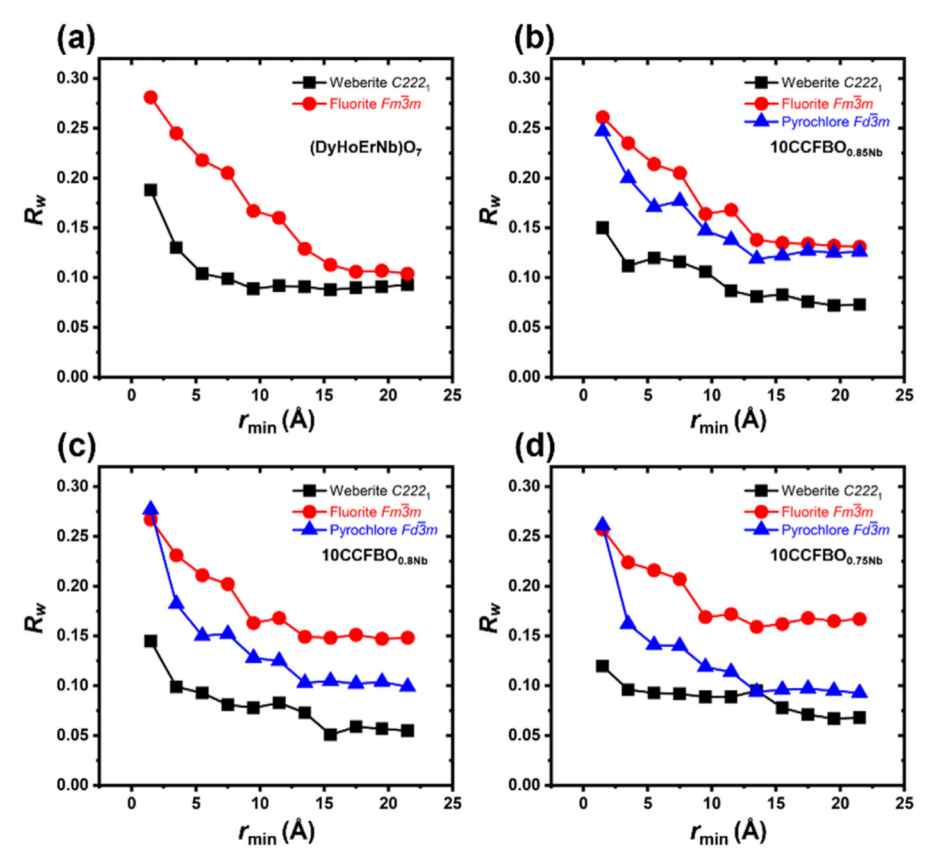


Fig. 5. Goodness-of-fit parameter (Rw) of four $10CCFBO_{xNb}$: (a) (DyHoErNb)O₇ (x ¼ 1), (b) $10\text{CCFBO}_{0.85\text{Nb}}$, (c) $10\text{CCFBO}_{0.8\text{Nb}}$, and (d) 10CCFBO_{0.75Nb} vs. different r-values based on "boxcar" refinements of the neutron PDFs using three structural models (Fd $\overline{3}$ m, Fm $\overline{3}$ m and C222₁). The r_{min} represents the minimum r-value of each 10 Å fit window (e.g., 1.5-11.5 Å). For (DyHoErNb)O₇, pyrochlore model generates huge errors (Rw > 0.8), so it was excluded. In general, the C2221 always generated better fitting compared other two structures (because of more fitting parameters), while the dependence on the r_{min} value provides more insights. As r_{min} increases, the fitting errors for the Fd 3 m (x 1/4 0.75 and 0.8) and Fm $\overline{3}$ m (x $\frac{1}{2}$ 0.85 and 1) tend to converge and approach to the C2221 fitting.

pyrochlore structure. No secondary phase was detected in XRD (Fig. 1a) or EDS elemental mapping (Suppl. Fig. S1). There is an ODT from ordered pyrochlore to disordered defect fluorite structure between 10CCFBO_{0.8Nb} and 10CCFBO_{0.812Nb}, evident by the vanished (331)_p superstructure peak in Fig. 1b. Here, we monitor the ODT via examining the (331)_p peak, which has the highest intensity among the pyrochlore superstructure peaks. To further exclude the possible existence of fluorite and pyrochlore dual-phase region, SEM/EDS was applied to check the elemental homogeneity of 10CCFBO_{xNb}, as shown in Suppl. Fig. S1. The images were taken by backscattered electron on polished pellet samples and EDS mapping showed homogeneous elemental distribution with no detectable secondary phase in all samples examined. The nanoscale elemental homogeneity was further confirmed by STEM based EDS elemental mapping, as shown in Suppl. Fig. S2 at the length scale of ~20-100 nm (including a grain boundary) and Fig. 1c at the atomic scale (noting that the compositional inhomogeneity at ~1 nm scale cannot be measured by STEM EDS since the TEM specimen thickness is > 20 nm; thus, the variations in the EDS intensities at ~1 nm scale are likely due to measurement noises and statistical fluctuations at the atomic scale). Combining both microscale and nanoscale EDS mapping and XRD patterns confirms the formation of single-phase 10CCFBO with homogenous chemical distribution, to the best that we can reasonably characterize.

We recognize that inhomogeneous distribution of metal elements caused by chemical short-range ordering (noting that it differs from the weberite-type structural short-range disordering) likely exist in these 10CCFBOs. However, it is extremely challenging, if not infeasible, to directly characterize such compositional inhomogeneity at $\sim\!1\,$ nm scale in these specimens with 10 different metal cations. For example, STEM EDS mapping averages the composition along the TEM specimen thickness direction (for at least >20 nm) so that the compositional inhomogeneity at $\sim\!1\,$ nm scale cannot be measured by the EDS elemental maps. Nonetheless, such compositional inhomogeneity caused by

chemical short-range ordering likely exists, and it can further interact with long- and short-range structural orders to produce new and interesting phenomena.

The finding that the ODT takes place between x % 0.8 and 0.812 (where the percentage differences in many elements are close to errors so we cannot probe finer compositional step) without observable dualphase region is somewhat a surprise. This finding in 10-component oxides (10CCFBO_{xNb}) is also in contrast to prior reports of a similar ODT in simpler Ho₂Ti_{2-y}Zr_yO₇, which suggested a pyrochlore and defect fluorite coexisting dual-phase region during ODT at y ~ 1.2 [15,20]. In a 10component system, the Gibbs phase rule allows the co-existence of up to 10 phases at equilibrium. Yet, this series of 10CCFBO_{xNb} specimens all possess single-phase, where a pyrochlore-fluorite phase transformation occurs with increasing compositional variable x abruptly without a detectable dual-phase (or multi-phase) region. This may be related to the so-called "high-entropy effect" (i.e., the stabilization a single solid-solution phase due to its high configurational entropy [56-58]) that reduces or suppresses the dual- or multi-phase region (that will have lower configurational entropies). However, the underlying mechanism needs to be further investigated via thermodynamic modeling (that is non-trivial for a 10-component system and beyond the scope of this work).

3.2. Atomistic mechanism of the long-range ODT

To analyze the atomic level mechanism of the long-range ODT, we conducted neutron diffraction experiments at VULCAN, at SNS, ORNL. Ten $10\text{CCFBO}_{\text{xNb}}$ specimens were tested in a sequence at 290 K in air for structural analysis. Fig. 2a shows all neutron diffraction patterns of the $10\text{CCFBO}_{\text{xNb}}$ series with a transition from pyrochlore to defect fluorite structure. Within the enlarged region of pyrochlore (331)_p and (511)_p superstructure peaks shown in Fig. 2b, the intensity of superstructure

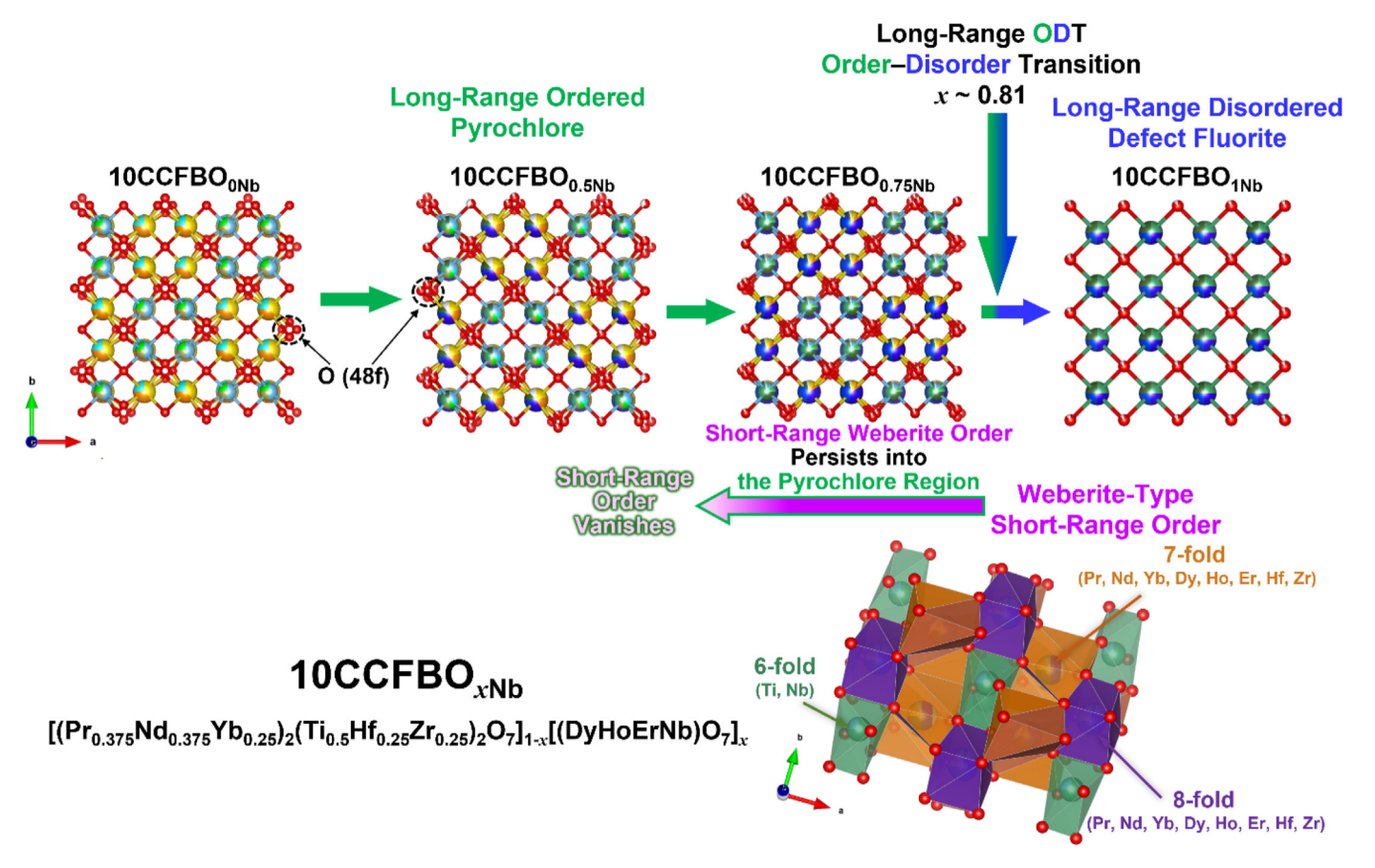
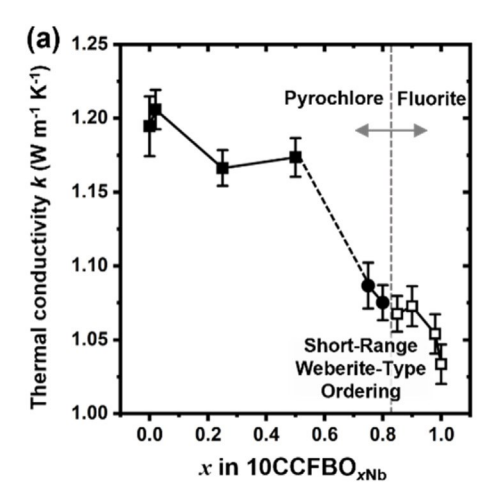


Fig. 6. Illustration of the transitions and competition of the long-range and short-range ordering vs. disordering in the 10CCFBO_{xNb} series. The crystal structures are plotted based on the refinements of the neutron diffraction patterns. The red spheres stand for oxygen anions and the white portion in red sphere shows the fractions of oxygen vacancies for the long-range structure.



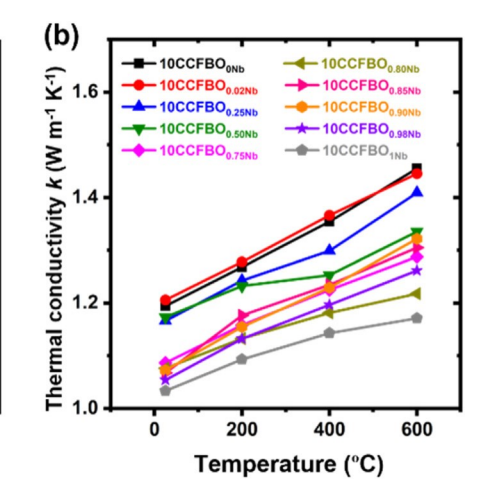


Fig. 7. (a) Room temperature thermal conductivity vs. x in the $10\text{CCFBO}_{x\text{Nb}}$ series of specimens. The solid squares stand for the long-range pyrochlore phases without short-range weberite-type ordering and solid circles represent the compositions with long-range pyrochlore phases with short-range weberite-type ordering. The hollow squares stand for long-range defect fluorite phases with short-range weberite-type ordering. The error bars are calculated based on the standard deviations of five individual measurements. (b) Temperature-dependent thermal conductivity curves for all $10\text{CCFBO}_{x\text{Nb}}$ specimens.

peaks gradually decreases and completely vanishes after x > 0.8, which confirms the ODT observed from XRD. In the neutron diffraction, the $10\text{CCFBO}_{x\text{Nb}}$ near the ODT ($x \ 10^{\circ}$ 0.75, 0.8, 0.85, 0.9, 0.98, and 1) also show diffuse scattering background peaks near the pyrochlore $(331)_p$ and $(511)_p$ peaks (but a careful analysis later suggests that they are not from pyrochlore ordering, but from short-range weberite ordering). These diffuse scattering background indicates short-range ordering in these $10\text{CCFBO}_{x\text{Nb}}$, akin to previously reported fluorite systems [9,16,59], which will be discussed in detail later.

The atomic level long-range structural evolution was analyzed by

Rietveld refinements of the neutron diffraction patterns. For the pyrochlore (Fd $\overline{3}$ m) structure, we chose to maintain an exact A:B ratio (1:1) and designate the larger ions to occupy A sites and smaller ions to take the B sites. Thus, the general ordered chemical formula for the $A_2B_2O_7$ pyrochlore can be written as:

$$\begin{split} &[(Pr_{0.375}Nd_{0.375})_{1-x}(Dy_{0.5}Ho_{0.5})_xEr_{x/2}Yb_{(1-3x)/4}]_2[Yb_x(-Ti_{_{0.5}}Hf_{0.25}Zr_{0.25})_{1-x}Nb_{x/2}]_2O_7 \text{ for } x<1/3 \text{ or } \\ &[(Pr_{0.375}Nd_{0.375})_{1-x}(Dy_{0.5}Ho_{0.5})_xEr_{(1-x)/4}]_2[Er_{(3x-1)/4}Yb_{(1-x)/4}]_2(Ti_{_{0.5}}Hf_{0.25}Zr_{_{0.25}})_{1-x}Nb_{x/2}]_2O_7 \text{ for } x>1/3. \end{split}$$

To further verify this hypothesized configuration, we conducted Rietveld refinements of the neutron diffraction assuming several different cation arrangements, which all produced larger fitting errors (Suppl. Fig. S3). For example, the ordered pyrochlore structure of $10\text{CCFBO}_{0.8\text{Nb}}$ has the ideal configuration of $(\text{Pr}_{0.075}\text{Nd}_{0.075}\text{Dy}_{0.4}\text{Ho}_{0.4}\text{Er}_{0.05})_2(\text{Hf}_{0.05}\text{Ti}_{0.1}\text{Zr}_{0.05}\text{Nb}_{0.4}\text{Er}_{0.35}\text{Yb}_{0.05})_2\text{O}_7$ (albeit some inevitable anti-site defects due to entropic effects). This structure can preserve exact A:B (1:1) stoichiometry and generate the best refinement fittings (with weighted profile residual R_w 0.03).

In Rietveld refinements, cations on the A site were constrained to have the same isotropic atomic displacement parameters U_a as that for the B site (U_b) . For oxygen anions in the pyrochlore structure (Fd $\overline{3}$ m), there are three different positions: (1) 48f (u, 1/8, 1/8) (again, we used u here to differentiate x in $10\text{CCFBO}_{\text{XNb}}$); (2) 8b(3/8, 3/8, 3/8); (3) 8a(1/8, 1/8, 1/8) (vacant site). In the initial refinement of the pyrochlore endmember $(Pr_{0.375}\text{Nd}_{0.375}\text{Yb}_{0.25})_2(Ti_{0.5}\text{Hf}_{0.25}Zr_{0.25})_2O_7$, we assumed the O(48f) and O(8b) were fully occupied and O(8a) were fully vacant as a starting point. With increasing x in $10\text{CCFBO}_{\text{XNb}}$, the prior refinement results of oxygen anion parameters were used as an initial state for the subsequent compositions.

Fig. 2c displays an example refinement result of $10\text{CCFBO}_{0.5\text{Nb}}$ with a R_w % 0.031, where the experimental data can be well fitted by the cubic pyrochlore model. All other Rietveld refinement results were documented in Suppl. Fig. S4, which all produced low fitting errors. There are two important parameters to understand the pyrochlore to defect fluorite transition: (1) the positional parameter u of O(48f) and (2) the occupancy of O(8a) site. During the ODT, u will move towards 0.375 and O(8a) will reach 0.875, which were reported for simpler ternary or quaternary fluorite-based oxides [16,17,59].

Fig. 2d shows the evolution of the refined O(8a) site occupancy and O(48f) positional parameter u with increasing compositional variable x in 10CCFBO_{xNb}. The dense and hollow symbols represent the best fitted parameters in pyrochlore and defect fluorite, respectively. With increasing compositional variable x, the oxygen atoms at occupied O(48f) position appear to migrate to nominally vacant O(8a) site, and "fill" some vacant O(8a) sites (with increasing 8a occupancy), while O(8b) site is kept fully occupied. In pyrochlore structure, O(48f) and O(8a) are the nearest neighbors, so that the migration between those two sites is possible (Fig. 2e). As x increases from 0 to 0.8 near the ODT, the occupancy of O(8a) increases from 0 (for x 1/4 0) to 0.89 (for x 1/4 0.8, which is almost equal to the ideal value of 0.875 for defect fluorite) with an almost linear increase and apparently no discontinuous jump at the ODT. The positional parameter u of O(48f) increases from 0.330 (x 1/4 0) to 0.358 (x % 0.8) but with a rather abrupt jump from 0.358 (x % 0.8) to 0.375 (x 1/4 0.85) during the ODT. This behavior indicates that the oxygen anions need to cross an energy barrier during the ODT. Thus, the ODT is likely a discontinuous phase transformation (with an order parameter vanished discontinuously).

3.3. Unique character of the ODT and unusual phase stability

On the one hand, our 10-component 10CCFBO_{xNb} series behave similarly in terms of oxygen anion movement during the long-range ODT as that reported for simpler 3-component Y₂(Zr_yTi_{1-y})₂O₇ [16,59]. The oxygen anion migration remains the key for the long-range ODT in this series of 10-component oxides, regardless of the ultrahigh-entropy compositions. On the other hand, one interesting difference between our 10CCFBO_{xNb} and simpler quaternary systems is that there is no observable dual-phase region (coexistence of defect fluorite and pyrochlore) to the best that we can characterize. Such dual-phase regions were suggested for Ho₂(Zr_yTi_{1-y})₂O₇ [20] and Y₂(Sn_yZr_{1-y})₂O₇ [9]. In contrast, there was no detectable phase separation in 10CCFBO_{xNb} by neutron diffraction, XRD, and EDS elemental mapping in different length scales (Figs. 1 and 2 and Supplementary Fig. S1-S2). However, we note that diffuse scattering of weberite-type shorting-range ordering was

observed in both ordered pyrochlore 10CCFBO $_{xNb}$ (x % 0.75 and 0.8) and disordered defect fluorite structures (Suppl. Fig. S5), which will be discussed in the subsequent section.

To further analyze the character of this long-range ODT in 10CCFBO_{xNb}, we plotted the normalized peak area of (331)_p vs. x from both neutron diffraction and XRD patterns (Fig. 3a). The diffuse scattering identified (Suppl. Fig. S5) was also fitted as a single Gaussian/ Lorentz peak, and the 1/FWHM (reciprocal Full Width Half Maximum) was calculated and also shown in Fig. 3a. We note that the integrated peak area of (331)_n has a virtually linear relation with compositional variable x for both neutron diffraction and XRD results ($R^2 \frac{1}{4} \sim 0.99$); the extrapolated x value of zero peak area was found to be 0.82 0.02 for neutron diffraction and 0.87 0.03 for XRD, respectively. Fig. 3b displays the enlarged region of the ODT and the hollow symbols stood for 10CCFBO_{xNb} with defect fluorite structure, for which the area of (311)_p was set to 0. The ODT can be narrowed down to 0.81 0.01 (between 0.8 and 0.812 according to XRD shown in Fig. 1). A close-up shown in Fig. 3b also suggests a rather abrupt vanishing of (331)_p superstructure peak intensity near the ODT, deviated from the linear extrapolation of peak intensities far away from the actual ODT. Thus, both neutron diffraction and XRD exhibit an abrupt (accelerated) disappearance of the (331)_p peak at the ODT (at x ¼ 0.81 0.01, vs. 0.82 and 0.87 projected from linear extrapolations). This observation can be explained from the abrupt O(48f) migration during the ODT revealed by Rietveld refinements of the neutron diffraction patterns (Fig. 2d). It again suggests that this ODT is likely discontinuous phase transformation, where an order parameter (e.g., that represented by the superstructure peak intensity) vanishes discontinuously at the ODT). In summary, the long-range order of 10CCFBO_{xNb} vanishes almost continuously with increasing x, but with a final small abrupt (discontinuous) transition at the ODT that can be attributed to a small jump of the O(48f) position (Fig. 2e).

Interestingly, as x decreases from 0.85 to 0.8 (passing through ODT with the merging of long-range pyrochlore order), a concurrent decrease of the 1/FWHM in the diffuse scattering is observed, which may represent the shrinkage of the domain (coherent) size of the short-range weberite-type order (discussed later) as a result of the interaction with the long-range pyrochlore order.

Prior studies suggested the ionic radii ratio (r_A/r_B) can determine the pyrochlore vs. fluorite phase stability in ternary A₂B₂O₇ (with ordered pyrochlore forming at $r_A/r_B > 1.46$) [60]. In the 10CCFBO_{xNb} series, rðAÞ/rðBÞ was calculated based on the chemical formula discussed above assuming that Yb^{3b} and Er^{3b} occupy the B site to keep an exact 1:1 ratio of A:B. The weighted average ionic radii ratio $\overline{r}\overline{\delta}AP/\overline{r}\overline{\delta}BP$ vs. x for the 10CCFBO_{xNb} series is shown in Suppl. Fig. S6. As x increases, the averaged ionic radii ratio (roAP/roBP) decreases. Compared to the pyrochlore formation threshold of $r_A/r_B > \sim 1.46$ in simpler $A_2B_2O_7$ ternary oxides, the 10CCFBO_{xNb} series show an ODT with a lower threshold of ~1.39 between 10CCFBO_{0.8Nb} and 10CCFBO_{0.85Nb}. This appears to even more surprising as we have Yb^{3 β} and Er^{3 β} occupy the B site in 10CCFBO_{xNb}, which intuitively should make the ordered pyrochlore structure unstable (prone to disorder). In most pyrochlores, larger sized rare earth elements usually occupy A site and smaller transition metal elements like Ti and Zr occupy B site. Thus, in the proposed model for 10CCFBO_{xNb}, large size Yb^{3b} and Er^{3b} dwell at the B site to maintain exact A:B stoichiometry. Hence, $\overline{r}\overline{\delta}BP$ has a larger value compared to the ionic radii of Zr and Hf in the typical ternary oxides [60].

We also calculated the ionic radii and molar ratio between all rare earth elements (RE ½ Pr^{3b} , Nd^{3b} , Yb^{3b} , Dy^{3b} , Ho^{3b} , and Er^{3b}) and all other transition metal elements (TM ½ Ti^{4b} , Zr^{4b} , Hf^{4b} and Nb^{5b}). Fig. 3c shows the molar ratio X_{RE}/X_{TM} vs. ionic radii ratio $\overline{r_{RE}}/\overline{r_{TM}}$ for the $10CCFBO_{xNb}$ series, along with those for three selected ternary $RE_2Hf_2O_7$ hafnates. For ternary hafnates, there are two phase boundary compositions (denoted at "Pb" and "Fb" for the rare earth element rich side of dual-phase tie-line), representing the equilibrium pyrochlore and fluorite compositions in the pseudo-binary phase diagram; see Fig. 3d for an

example of $Gd_2Hf_2O_7$ (replotted after ACerS-NIST phase diagram No. 9299). For these ternary hafnates, the molar ratio range of the dual-phase (F \flat P)region increases with the ionic radii ratio $r_{RE}=r_{TM}$. In contrast, the $10CCFBO_{xNb}$ series has a virtually abrupt phase transition (ODT) between $10CCFBO_{0.8Nb}$ and $10CCFBO_{0.812Nb}$ without an observable (F \flat P) dual-phase region. This again suggests the uniqueness of this abrupt ODT (lacking a discernible dual-phase region) in the 10-component CCFBOs, deviating from the projection from ternary oxides (Fig. 3).

3.4. Short-range order and its interaction with long-range ODT

Diffuse scattering was found in $10\text{CCFBO}_{x\text{Nb}}$ near the ODT (for x ½ 0.75, 0.8, 0.85, 0.9, 0.98, and 1), which can be attributed to nanoscale weberite-type ordering (akin to those observed in simple oxides [14,61,62]), based on analysis of the peak position and its shift (Fig. 3e), which are further confirmed by small-box modeling (discussed later). Interestingly, the short-range order can form in both disordered defect fluorite (x ½ 0.85, 0.9, 0.98, and 1) and barely ordered pyrochlore (x ½ 0.75 and 0.8).

To further illustrate this interaction, both the (331)_p peaks in the pyrochlore structure (for x ¼ 0, 0.25, 0.5, 0.75, and 0.8) and the diffuse scattering for weberite-type short-range ordering (for x ¼ 0.75, 0.8, 0.85, 0.9, 0.98, and 1), respectively, were fitted as single Gaussian and Lorentz peaks, respectively. The peak position vs. x is displayed in Fig. 3e. The square and circle symbols, respectively, in Fig. 3e stand for the positions of (331)_p and diffuse scattering, respectively. The reciprocal peak width (1/FWHM) vs. x of the fitted diffuse scattering is shown in Fig. 3a.

As shown in Fig. 3e, the peak position of (331)_p undergoes a small increase with increasing x, which follows the same trend as in the measured lattice parameter because the defect fluorite endmember (DyHoErNb)O₇ has the larger lattice parameter than the pyrochlore endmember (Pr_{0.375}Nd_{0.375}Yb_{0.25}) (Ti_{0.5}Hf_{0.25}Zr_{0.25})O₇ (Fig. 3f). During the ODT (x ½ 0.8 to 0.85), the (331)_p peak disappears, and peak position of the diffuse scattering moves slightly towards the higher d spacing. The appreciable position difference of (331)_p peak (d ½ 2.407 Å) and diffuse scattering (d ½ 2.35 Å) at x ½ 0.8 suggests that the diffuse scattering cannot be attributed to broadening of the (331)_p peaks, but it may represent weberite-type short-range ordering (e.g., the (041) peak in the weberite-type structure C222₁ that broadens and merges with other peaks to become diffuse scattering).

Passing the ODT into ordered pyrochlore region with reducing x, the short-range order interacts with the long-range order, resulting in changes in both the width (Fig. 3a, implying reduced domain sizes in long-range ordered region) and position (Fig. 3e, virtually continuous at ODT, but with an altered slope with varying x) of the diffuse scattering.

To further confirm hypothesized weberite-type short-range ordering in $10\text{CCFBO}_{\text{NNb}}$ more directly, we conducted neutron total scattering to probe the compositions near the ODT (x ½ 0.75, 0.8, 0.85, and 1) using the Nanoscale-Ordered Materials Diffractometer NOMAD (SNS, ORNL), which offer much improved sensitivity to probe short-range orders (in comparation with conventional neutron diffraction). The total radial distribution function G(r) is obtained by Fourier transform of the structure factor, S(Q) for further analysis.

Fig. 4a shows neutron diffraction data from bank 3 of the NOMAD in $(331)_p$ peak region for four 10CCFBO_{xNb} compositions (x ¼ 0.75, 0.8, 0.85 and 1) near the ODT. Here, clearer diffuse scattering can be observed for all four compositions. The diffuse scattering of $10\text{CCFBO}_{0.75\text{Nb}}$ and $10\text{CCFBO}_{0.8\text{Nb}}$ were plotted by fitted Chebyshev backgrounds. Notably, no diffuse scattering can be observed at the $(331)_p$ region when x reaches 0.5 (Suppl. Fig. S7), suggesting the vanishing of the short-range order. Neutron pair distribution functions (PDFs) of the $10\text{CCFBO}_{x\text{Nb}}$ series (Fig. 4b) can provide information of short-range atomic arrangement. As x increases, the peaks at larger r values (r > 15 Å) slightly shift to higher r, which corresponds to the expansion of unit cell in concert with lattice parameters measured by conventional neutron diffraction at the Vulcan diffractometer (Fig. 3f).

For the peaks at small r values (<10 Å), all four compositions exhibit similar curve shapes, which suggest similar first and second nearest neighbors' environments. On a close look, the intensity of peak at around 1.95 Å decreases as x decreases.

To investigate this local structural evolution, small-box modelling was conducted using the PDFgui software. For each composition, three structural models were used to fit the PDFs: (1) pyrochlore (Fd $\overline{3}$ m), (2) defect fluorite (Fm $\overline{3}$ m), and (3) weberite-type (C222₁) structures. The same pyrochlore and defect fluorite models from previous refinements of longrange structure were adapted here for small-box modelling as the initial structures. For the weberite-type structure (A₃BO₇), we tried several combinations. The best fitting is achieved with the smallest error when Ti and Nb occupied the B site with coordination number of 6. For example, 10CCFBO_{0.75Nb} can be modeled as: (Pr_{0.0625}Nd_{0.0625} $Yb_{0.0417}Dy_{0.25}Ho_{0.25}Er_{0.25}Hf_{0.0417}Zr_{0.0417})_3(Ti_{0.25}Nb_{0.75})O_7$. The modeling results of other combinations with substantially larger errors were documented in Suppl. Fig. S8 for comparison. Notably, only the weberite-type structure can depict the low r region (<10 Å) with the small errors (Suppl. Fig. S9-S10). Neither pyrochlore nor defect fluorite model can produce the 1.95 Å peak. This suggests the presence of short-range weberite-type

Fig. 4c displays the small-box modeling of all four compositions (x 1/4 0.75, 0.8, 0.85, and 1) with the weberite-type C222₁ structure. The good fitting further confirmed the short-range ordering at smaller length scales (deviated from the long-range pyrochlore or defect fluorite ordering). Fig. 4d shows the partial PDFs for several major bonds fitted with the weberite-type C222₁ structure in 10CCFBO_{0.75Nb}, where M stands for all elements occupying the A site (Pr, Nd, Dy, Ho, Er, Yb, Hf and Zr) in A₃BO₇. The Nb-O and Ti-O signatures both locate at around 1.95 Å with opposite neutron scattering. As x decreases from 1 to 0.75, Ti gradually replaces with Nb on B site for weberite-type structure, which correlates well with the decreasing peak intensity at r $\mbox{\upmu}$ 1.95 Å. Additional partial PDFs results were shown in Suppl. Fig. S11. "Boxcar" refinement was applied to examine the short-range ordering deviation from the overall structure (Fig. 5) [20,63]. In general, the weberite-type C222₁ structure can produce better fitting results. In contrast, the exclusion of r-range below 5 Å that contained the first and second nearest neighbor polyhedral and coordination substantially improved the Rw of the pyrochlore and defect fluorite structural fitting. As rmin further increases, both pyrochlore and defect fluorite fittings converge to values comparable to that of the weberite-type structure fitting. The pyrochlore structure fits better for 10CCFBO_{0.75Nb} and 10CCFBO_{0.8Nb}, which is consistent with the analysis of long-range ordering above. For 10CCFBO_{0.85Nb}, the pyrochlore and defect fluorite generated similar R_w values because this composition is near the ODT. Note that the defect fluorite endmember (DyHoErNb)O7 (that has a long-range fluorite order with strong short-range weberite order) cannot be modeled as a pyrochlore structure with a reasonable error, which is consistent with our hypothesis.

As x increases in 10CCFBO_{xNb}, the movement of O(48f) to vacant O(8a) can create a new local coordination environment. To accommodate the charge balance induced by this oxygen anion migration, some of the cations should adopt a change in the coordinated configuration, e.g. Zr adopts a 7-, instead of 6-, coordinated configuration, which can lead to the local weberite-type structure [64-67]. In the weberite-type order in the C222₁ (A₁A₂BO₇) structure, A₁ is 8-, A₂ is 7- and B is 6-fold coordinated. In niobate systems, Nb tends to occupy the 6-coordinated B site in local ordering [25]. Ti also prefers the B site due to its smallest ionic radii. Other cations in 10CCFBO_{xNb} likely distribute in the A₁ and A₂ sites evenly. Compared to pyrochlore and defect fluorite structures, weberite-type ordering has more flexibility to tune the atomic positions for both cations and oxygen anions, which enables more flexibility of the local coordination environment change due to oxygen anion migration near the long-range ODT. In other words, the interplay of the short-range weberite-type ordering with long-range ODT is important.

The competition of long-range ODT and short-range ordering is

schematically illustrated in Fig. 6, based on the Rietveld refinements of the neutron diffraction patterns and small-box modelling of PDFs. In the $10\text{CCFBO}_{x\text{Nb}}$ series, the ordering vs. disordering may be decoupled in two different length scales. For long-range ordering (x from 0 to 0.5 to 0.75), the migration of O(48f) gradually alters the pyrochlore structure (Fig. 2d) and finally triggers a long-range ODT at around x ½ 0.81 to form disordered defect fluorite for the long-range order. As x increases from 0.5 to 0.75, where the long-range order is still ordered pyrochlore, weberite-type short-range order forms with Ti/Nb occupying the 6-coordinated site and all other cations evenly distributed among 7- and 8-coordinated sites. The weberite-type short-range ordering persists into the long-range defect fluorite structure after the ODT, but gradually vanishes at smaller x values.

Here, we acknowledge the possible anti-site mixing of cations on the A vs. B sites, which is inevitable due to an entropy effect, and it can be pronouncing near the ODT. In our pyrochlore structure model for the Rietveld refinements, the cation position is fixed, which is a simplification since anti-site disordering can also occur during the ODT. However, it is infeasible to capture this scenario with 10 different cations (including similar rare earth elements) the Rietveld refinements.

3.5. Thermal conductivity

Fig. 7a shows the room temperature thermal conductivity of 10CCFBO_{xNb}. In general, the thermal conductivity shows a decreasing trend with increasing x. Around the long-range ODT (for x between 0.8 and 0.85), the change of thermal conductivity was (surprisingly) small (comparable to the error bars). However, the short-range weberite-type ordering was present in 10CCFBO_{0.75Nb} and 10CCFBO_{0.8Nb}, as shown by diffuse scattering and the following PDFs data analysis showed the phase transformation (Figs. 2 and 4). No obvious diffuse scattering beneath (331)_p diffraction peak of 10CCFBO_{0.5Nb} was observed (Suppl. Fig. S7), which suggests that the short-range transformation took place in between 10CCFBO_{0.5Nb} and 10CCFBO_{0.75Nb}. Interestingly, a larger drop in the thermal conductivity takes place in between 10CCFBO_{0.5Nb} and 10CCFBO_{0.75Nb} from 1.17 W m¹EK¹ to 1.08 W m¹EK¹ (in contrast to a smaller 1.05 W m¹ EK¹ to 1.07 W m¹ EK¹ change in between 10CCFBO_{0.8Nb} and 10CCFBO_{0.85Nb} for the long-range ODT). Thus, we hypothesize that the formation of weberite-type local structure (shortrange ordering) can more appreciably alter thermal conductivity in 10CCFBO_{xNb} (in comparison with the long-range pyrochlore-to-fluorite ODT). It was proposed that the thermal conductivity can be significantly affected by the formation of dispersed nanodomains [68]. Prior studies also found that the weberite-type short-range ordering can lower the thermal conductivity in high-entropy rare earth niobates and tantalates [25].

The temperature dependent thermal conductivity of $10\text{CCFBO}_{x\text{Nb}}$ shows an amorphous-like trend (Fig. 7b), where the thermal conductivity primarily increases with temperature due to increasing heat capacity.

4. Conclusions

In summary, we have investigated the long-range vs. short-range ordering and disordering, as well as the interplays between them, in a 10-component compositionally complex oxide system at different length scales by combining neutron diffraction and neutron total scattering. The synthesized compositions all exhibit nominally single high-entropy phases with either defect fluorite or pyrochlore in their long-range order. Rietveld refinements of long-range atomic configurations based on neutron diffraction shows a continuous oxygen anion migration from fully occupied 48f to vacant 8a sites with increasing x in 10CCFBO_xNb, following a final jump during the long-range ODT at x ½ 0.81 0.01, while the 8a oxygen occupancy increases almost linearly without an apparent discontinuous jump at the ODT.

As a notable and interesting discovery, the long-range ODT takes place in the 10-component ultrahigh-entropy 10CCFBO_{xNb} without a

detectable dual- or multi-phase region, in contrast to the simpler 3- and 4-component oxides. The pyrochlore vs. fluorite phase stability of the 10-component ultrahigh-entropy 10CCFBO_{xNb} does not follow the criteria that are well established based on simpler 3- and 4-componnent oxides.

The coexistence of $(331)_p$ and diffuse scattering in $10\text{CCFBO}_{0.75\text{Nb}}$ and $10\text{CCFBO}_{0.8\text{Nb}}$ show the coexistence and competition of long-range pyrochlore order and short-range weberite-type order in these specimens. Four Nb-rich $10\text{CCFBO}_{\text{NNb}}$ (x % 0.75, 0.8, 0.85, and 1) near the ODT maintain similar local polyhedral environments when r < 10 Å, which can only be well fitted with the weberite-type structure $C222_1$ with the small-box modeling. The further "boxcar" refinements indicate that pyrochlore and defect fluorite can describe the structure well, if and only if the first and second nearest neighbor environment (r < 5 Å) is excluded. The combination of these analyses suggests the existence of short-range weberite-type order that overlaps and interplays with the long-range ODT in both ordered pyrochlore and disordered fluorite regions.

The room temperature thermal conductivity only has a negligible change during long-range ODT, but an appreciable drop when the short-range weberite-type ordering appears. This suggests that nanodomain structural distortion (short-range ordering) can reduce thermal conductivity more appreciably than the long-range ODT. In a broader context, elucidating and controlling the short- and long-range ordering vs. disordering may open a new window to tailor the structure, stability, and properties of HECs and CCCs with substantial compositional disorder (high configurational entropy).

Declaration of competing interest

The authors declare that they have no known competing financial interests or personal relationships that could have appeared to influence the work reported in this paper.

Acknowledgement

The work is supported by the National Science Foundation (NSF) via Grant No. DMR-2026193. A portion of this research used resources at the Spallation Neutron Source, a DOE Office of Science User Facility operated by the ORNL. The STEM work was performed at the Irvine Materials Research Institute (IMRI).

Appendix A. Supplementary data

Supplementary data to this article can be found online at https://doi.org/10.1016/j.apmate.2022.100098.

References

- D. Ding, X. Li, S.Y. Lai, K. Gerdes, M. Liu, Enhancing SOFC cathode performance by surface modification through infiltration, Energy Environ. Sci. 7 (2014) 552, https://doi.org/10.1039/c3ee42926a.
- [2] N. Mahato, A. Banerjee, A. Gupta, S. Omar, K. Balani, Progress in material selection for solid oxide fuel cell technology: a review, Prog. Mater. Sci. 72 (2015) 141–337, https://doi.org/10.1016/J.PMATSCI.2015.01.001.
- [3] E.R. Andrievskaya, Phase equilibria in the refractory oxide systems of zirconia, hafnia and yttria with rare-earth oxides, J. Eur. Ceram. Soc. 28 (2008) 2363–2388, https://doi.org/10.1016/j.jeurceramsoc.2008.01.009.
- [4] V. Ponnilavan, A. Aravind, M. Ezhilan, S. Kannan, Titanium substitution in Gd₂Zr₂O₇ for thermal barrier coating applications, Ceram. Int. 45 (2019) 16450–16457, https://doi.org/10.1016/J.CERAMINT.2019.05.176.
- [5] X.G. Chen, A. Tang, H.S. Zhang, Y.X. Liu, H.M. Zhang, Y.D. Zhao, Thermal conductivity and expansion coefficient of Ln2LaTaO₇ (Ln½Er and Yb) oxides for thermal barrier coating applications, Ceram. Int. 42 (2016) 13491–13496, https:// doi.org/10.1016/J.CERAMINT.2016.05.141.
- [6] J. Shamblin, M. Feygenson, J. Neuefeind, C.L. Tracy, F. Zhang, S. Finkeldei, D. Bosbach, H. Zhou, R.C. Ewing, M. Lang, Probing disorder in isometric pyrochlore and related complex oxides, Nat. Mater. 15 (2016) 507–511, https://doi.org/ 10.1038/nmat4581.
- [7] K.E. Sickafus, R.W. Grimes, J.A. Valdez, A. Cleave, M. Tang, M. Ishimaru, S.M. Corish, C.R. Stanek, B.P. Uberuaga, Radiation-induced amorphization

- resistance and radiation tolerance in structurally related oxides, Nat. Mater. 6 (2007) 217–223, https://doi.org/10.1038/nmat1842.
- [8] K.E. Sickafus, L. Minervini, R.W. Grimes, J.A. Valdez, M. Ishimaru, F. Li, K.J. McClellan, T. Hartmann, Radiation tolerance of complex oxides, Science 289 (2000) 748–751, https://doi.org/10.1126/SCIENCE.289.5480.748.
- [9] Z. Zhang, S.C. Middleburgh, M. De Los Reyes, G.R. Lumpkin, B.J. Kennedy, P.E.R. Blanchard, E. Reynolds, L.Y. Jang, Gradual structural evolution from pyrochlore to defect-fluorite in Y₂Sn_{2-x}Zr_xO₇: average vs local structure, J. Phys. Chem. C 117 (2013) 26740–26749, https://doi.org/10.1021/jp408682r.
- [10] P.S. Maram, S.V. Ushakov, R.J.K. Weber, C.J. Benmore, A. Navrotsky, Probing disorder in pyrochlore oxides using in situ synchrotron diffraction from levitated solids-A thermodynamic perspective, Sci. Rep. 8 (2018) 1–11, https://doi.org/ 10.1038/s41598-018-28877-x.
- [11] L. Zhou, Z. Huang, J. Qi, Z. Feng, D. Wu, W. Zhang, X. Yu, Y. Guan, X. Chen, L. Xie, K. Sun, T. Lu, Thermal-driven fluorite-pyrochlore-fluorite phase transitions of Gd₂Zr₂O₇ ceramics probed in large range of sintering temperature, Metall. Mater. Trans. A 47 (2016) 623–630, https://doi.org/10.1007/811661-015-3234-4.
- [12] E.C. O'Quinn, C.L. Tracy, W.F. Cureton, R. Sachan, J.C. Neuefeind, C. Trautmann, M.K. Lang, Multi-scale investigation of heterogeneous swift heavy ion tracks in stannate pyrochlore, J. Mater. Chem. A. 9 (2021) 16982–16997, https://doi.org/ 10.1039/d1ta04924k.
- [13] C. Karthik, T.J. Anderson, D. Gout, R. Ubic, Transmission electron microscopic study of pyrochlore to defect-fluorite transition in rare-earth pyrohafnates, J. Solid State Chem. 194 (2012) 168–172, https://doi.org/10.1016/j.jssc.2012.05.008.
- [14] P.E.R. Blanchard, R. Clements, B.J. Kennedy, C.D. Ling, E. Reynolds, M. Avdeev, A.P.J. Stampfl, Z. Zhang, L.Y. Jang, Does local disorder occur in the pyrochlore zirconates? Inorg. Chem. 51 (2012) 13237–13244, https://doi.org/10.1021/ ic301677b
- [15] M. Shafique, B.J. Kennedy, Y. Iqbal, R. Ubic, The effect of B-site substitution on structural transformation and ionic conductivity in Ho₂(Zr_yTi_{1-y})₂O₂, J. Alloys Compd. 671 (2016) 226–233, https://doi.org/10.1016/j.jallcom.2016.02.087.
- [16] S.T. Norberg, S. Hull, S.G. Eriksson, I. Ahmed, F. Kinyanjui, J.J. Biendicho, Pyrochlore to fluorite transition: the Y₂(Ti_{1-x}Zr_x)₂O₇ (0.0 x 1.0) System, Chem. Mater. 24 (2012) 4294–4300, https://doi.org/10.1021/cm301649d.
- [17] R. Clements, J.R. Hester, B.J. Kennedy, C.D. Ling, A.P.J. Stampfl, The fluorite-pyrochlore transformation of Ho_{2-y}Nd_yZr₂O₂, J. Solid State Chem. 184 (2011) 2108–2113, https://doi.org/10.1016/j.jssc.2011.05.054.
- [18] J. Shamblin, C.L. Tracy, R.I. Palomares, E.C. O'Quinn, R.C. Ewing, J. Neuefeind, M. Feygenson, J. Behrens, C. Trautmann, M. Lang, Similar local order in disordered fluorite and aperiodic pyrochlore structures, Acta Mater. 144 (2018) 60–67, https://doi.org/10.1016/j.actamat.2017.10.044.
- [19] R. Sherrod, E.C. O'Quinn, I.M. Gussev, C. Overstreet, J. Neuefeind, M.K. Lang, Comparison of short-range order in irradiated dysprosium titanates, Npj Mater. Degrad. 5 (2021) 1–7, https://doi.org/10.1038/s41529-021-00165-6.
- [20] D.L. Drey, E.C. O'Quinn, T. Subramani, K. Lilova, G. Baldinozzi, I.M. Gussev, A.F. Fuentes, J.C. Neuefeind, M. Everett, D. Sprouster, A. Navrotsky, R.C. Ewing, M. Lang, Disorder in Ho₂Ti_{2-x}Zr_xO₇: pyrochlore to defect fluorite solid solution series, RSC Adv. 10 (2020) 34632–34650, https://doi.org/10.1039/d0ra07118h.
- [21] W. Hong, F. Chen, Q. Shen, Y.H. Han, W.G. Fahrenholtz, L. Zhang, Microstructural evolution and mechanical properties of (Mg, Co, Ni, Cu, Zn) O high-entropy ceramics, J. Am. Ceram. Soc. 102 (2019) 2228–2237, https://doi.org/10.1111/ icep.16075
- [22] S. Zhou, Y. Pu, X. Zhang, Y. Shi, Z. Gao, Y. Feng, G. Shen, X. Wang, D. Wang, High energy density, temperature stable lead-free ceramics by introducing high entropy perovskite oxide, Chem. Eng. J. 427 (2022), 131684, https://doi.org/10.1016/ J.CEJ.2021.131684.
- [23] Q. Yang, G. Wang, H. Wu, B.A. Beshiwork, D. Tian, S. Zhu, Y. Yang, X. Lu, Y. Ding, Y. Ling, Y. Chen, B. Lin, A high-entropy perovskite cathode for solid oxide fuel cells, J. Alloys Compd. 872 (2021), 159633, https://doi.org/10.1016/ JJALLCOM.2021.159633.
- [24] J. Gild, M. Samiee, J.L. Braun, T. Harrington, H. Vega, P.E. Hopkins, K. Vecchio, J. Luo, High-entropy fluorite oxides, J. Eur. Ceram. Soc. 38 (2018) 3578–3584, https://doi.org/10.1016/j.jeurceramsoc.2018.04.010.
- [25] A.J. Wright, Q. Wang, Y.T. Yeh, D. Zhang, M. Everett, J. Neuefeind, R. Chen, J. Luo, Short-range order and origin of the low thermal conductivity in compositionally complex rare-earth niobates and tantalates, Acta Mater. 235 (2022), 118056, https://doi.org/10.1016/j.actamat.2022.118056.
- [26] J. Zhu, X. Meng, J. Xu, P. Zhang, Z. Lou, M.J. Reece, F. Gao, Ultra-low thermal conductivity and enhanced mechanical properties of high-entropy rare earth niobates (RE3NbO7, RE ¼ Dy, Y, Ho, Er, Yb), J. Eur. Ceram. Soc. 41 (2021) 1052–1057, https://doi.org/10.1016/j.jeurceramsoc.2020.08.070.
- [27] Z. Zhao, H. Chen, H. Xiang, F.Z. Dai, X. Wang, W. Xu, K. Sun, Z. Peng, Y. Zhou, High entropy defective fluorite structured rare-earth niobates and tantalates for thermal barrier applications, J. Adv. Ceram. 9 (2020) 303–311, https://doi.org/10.1007/ s40145-020-0368-7.
- [28] A.J. Wright, Q. Wang, C. Huang, A. Nieto, R. Chen, J. Luo, From high-entropy ceramics to compositionally-complex ceramics: a case study of fluorite oxides, J. Eur. Ceram. Soc. 40 (2020) 2120–2129, https://doi.org/10.1016/ j.jeurceramsoc.2020.01.015.
- [29] A.J. Wright, C. Huang, M.J. Walock, A. Ghoshal, M. Murugan, J. Luo, Sand corrosion, thermal expansion, and ablation of medium- and high-entropy compositionally complex fluorite oxides, J. Am. Ceram. Soc. 104 (2021) 448–462, https://doi.org/10.1111/jace.17448.
- [30] K. Zhang, W. Li, J. Zeng, T. Deng, B. Luo, H. Zhang, X. Huang, Preparation of $(La_{0.2}Nd_{0.2}Sm_{0.2}Gd_{0.2}Yb_{0.2})_2Zr_2O_7 \ high-entropy \ transparent ceramic using$

- combustion synthesized nanopowder, J. Alloys Compd. 817 (2020), 153328, https://doi.org/10.1016/J.JALLCOM.2019.153328.
- [31] Z. Teng, L. Zhu, Y. Tan, S. Zeng, Y. Xia, Y. Wang, H. Zhang, Synthesis and structures of high-entropy pyrochlore oxides, J. Eur. Ceram. Soc. (2019), https://doi.org/ 10.1016/j.eplepsyres.2019.106192.
- [32] M. Qin, H. Vega, D. Zhang, S. Adapa, A.J. Wright, R. Chen, J. Luo, 21-Component compositionally complex ceramics: discovery of ultrahigh-entropy weberite and fergusonite phases and a pyrochlore-weberite transition, J. Adv. Ceram. 11 (2022) 641–655, https://doi.org/10.1007/s40145-022-0575-5.
- [33] J. Dąbrowa, M. Stygar, A. Mikuła, A. Knapik, K. Mroczka, W. Tejchman, M. Danielewski, M. Martin, Synthesis and microstructure of the (Co, Cr, Fe, Mn, Ni) 3O4 high entropy oxide characterized by spinel structure, Mater. Lett. 216 (2018) 32–36, https://doi.org/10.1016/j.matlet.2017.12.148.
- [34] J. Gild, Y. Zhang, T. Harrington, S. Jiang, T. Hu, M.C. Quinn, W.M. Mellor, N. Zhou, K. Vecchio, J. Luo, High-entropy metal diborides: a new class of high-entropy materials and a new type of ultrahigh temperature ceramics, Sci. Rep. 6 (2016), 37946, https://doi.org/10.1038/srep37946.
- [35] M. Qin, Q. Yan, H. Wang, C. Hu, K.S. Vecchio, J. Luo, High-entropy monoborides: towards superhard materials, Scripta Mater. 189 (2020) 101–105, https://doi.org/ 10.1016/j.scriptamat.2020.08.018.
- [36] M. Qin, Q. Yan, H. Wang, K.S. Vecchio, J. Luo, High-entropy rare earth tetraborides, J. Eur. Ceram. Soc. 41 (2021) 2968–2973, https://doi.org/10.1016/ j.jeurceramsoc.2020.12.019.
- [37] M. Qin, Q. Yan, Y. Liu, J. Luo, A new class of high-entropy M3B4 borides, J. Adv. Ceram. 10 (2021) 166–172, https://doi.org/10.1007/s40145-020-0438-x Research Article%0AISSN.
- [38] M. Qin, Q. Yan, Y. Liu, H. Wang, C. Wang, T. Lei, K.S. Vecchio, H.L. Xin, T.J. Rupert, J. Luo, Bulk high-entropy hexaborides, J. Eur. Ceram. Soc. 41 (2021) 5775–5781, https://doi.org/10.1016/j.jeurceramsoc.2021.05.027.
- [39] E. Castle, T. Csanadi, S. Grasso, J. Dusza, M. Reece, Processing and properties of high-entropy ultra-high temperature carbides, Sci. Rep. 8 (2018) 8609, https:// doi.org/10.1038/s41598-018-26827-1.
- [40] T.J. Harrington, J. Gild, P. Sarker, C. Toher, C.M. Rost, O.F. Dippo, C. McElfresh, K. Kaufmann, E. Marin, L. Borowski, P.E. Hopkins, J. Luo, S. Curtarolo, D.W. Brenner, K.S. Vecchio, Phase stability and mechanical properties of novel high entropy transition metal carbides, Acta Mater. 166 (2019) 271–280, https:// doi.org/10.1016/j.actamat.2018.12.054.
- [41] X. Yan, L. Constantin, Y. Lu, J.F. Silvain, M. Nastasi, B. Cui, Hf_{0.2}Zr_{0.2}Ta_{0.2}Nb_{0.2}Ti_{0.2})C high-entropy ceramics with low thermal conductivity, J. Am. Ceram. Soc. 101 (2018) 4486–4491, https://doi.org/10.1111/jace.15779.
- [42] J. Gild, J. Braun, K. Kaufmann, E. Marin, T. Harrington, P. Hopkins, K. Vecchio, J. Luo, A high-entropy silicide: (Mo0.2Nb0.2Ta0.2Ti0.2W0.2)Si2, J. Mater. (2019), https://doi.org/10.1016/j.jmat.2019.03.002.
- [43] Y. Qin, J.X. Liu, F. Li, X. Wei, H. Wu, G.J. Zhang, A high entropy silicide by reactive spark plasma sintering, J. Adv. Ceram. 8 (2019) 148–152, https://doi.org/10.1007/ s40145-019-0319-3.
- [44] O.F. Dippo, N. Mesgarzadeh, T.J. Harrington, G.D. Schrader, K.S. Vecchio, Bulk high-entropy nitrides and carbonitrides, Sci. Rep. 10 (2020), https://doi.org/ 10.1038/s41598-020-78175-8.
- [45] D. Moskovskikh, S. Vorotilo, V. Buinevich, A. Sedegov, K. Kuskov, A. Khort, C. Shuck, M. Zhukovskyi, A. Mukasyan, Extremely hard and tough high entropy nitride ceramics, Sci. Rep. 10 (2020) 1–8, https://doi.org/10.1038/s41598-020-76945-v.
- [46] X. Chen, Y. Wu, High-entropy transparent fluoride laser ceramics, J. Am. Ceram. Soc. 103 (2019) 750–756, https://doi.org/10.1111/jace.16842.
- [47] A.J. Wright, J. Luo, A step forward from high-entropy ceramics to compositionally complex ceramics: a new perspective, J. Mater. Sci. 55 (2020) 8812–9827, https:// doi.org/10.1007/s10853-020-04583-w.
- [48] H. Xiang, Y. Xing, F. zhi Dai, H. Wang, L. Su, L. Miao, G. Zhang, Y. Wang, X. Qi, L. Yao, H. Wang, B. Zhao, J. Li, Y. Zhou, High-entropy ceramics: present status, challenges, and a look forward, J. Adv. Ceram. 10 (2021) 385–441.
- [49] A.J. Wright, Q. Wang, C. Huang, A. Nieto, R. Chen, J. Luo, From high-entropy ceramics to compositionally-complex ceramics: a case study of fluorite oxides, J. Eur. Ceram. Soc. (2020), https://doi.org/10.1016/j.jeurceramsoc.2020.01.015.
- [50] S. Shivakumar, M. Qin, D. Zhang, C. Hu, Q. Yan, J. Luo, A new type of compositionally complex M5Si3 silicides: cation ordering and unexpected phase stability, Scripta Mater. 212 (2022), 114557, https://doi.org/10.1016/ j.scriptamat.2022.114557.
- [51] A.J. Wright, Q. Wang, C. Hu, Y.T. Yeh, R. Chen, J. Luo, Single-phase duodenary high-entropy fluorite/pyrochlore oxides with an order-disorder transition, Acta Mater. 211 (2021), 116858, https://doi.org/10.1016/j.actamat.2021.116858.
- [52] D. Zhang, Y. Chen, T. Feng, D. Yu, K. An, R. Chen, J. Luo, Discovery of a reversible redox-induced order-disorder transition in a 10-component compositionally complex ceramic, Scripta Mater. 215 (2022), 114699, https://doi.org/10.1016/ i.scriptamat.2022.114699.
- [53] B. Jiang, C.A. Bridges, R.R. Unocic, K.C. Pitike, V.R. Cooper, Y. Zhang, D.Y. Lin, K. Page, Probing the local site disorder and distortion in pyrochlore high-entropy oxides, J. Am. Chem. Soc. 143 (2021) 4193–4204, https://doi.org/10.1021/ jacs.0e10739.
- [54] K. An, Y. Chen, A.D. Stoica, Vulcan, VULCAN: a "hammer" for high-temperature materials research, MRS Bull. 44 (2019) 878–885, https://doi.org/10.1557/ mrs.2019.256.
- [55] R.W. Rice, Porosity of Ceramics: Properties and Applications, CRC Press, 1998.
- [56] D.B. Miracle, O.N. Senkov, A critical review of high entropy alloys and related concepts, Acta Mater. 122 (2017) 448–511, https://doi.org/10.1016/ j.actamat.2016.08.081.

- [57] J.W. Yeh, Alloy design strategies and future trends in high-entropy alloys, JOM (J. Occup. Med.) 65 (2013) 1759–1771, https://doi.org/10.1007/s11837-013-0761-6.
- [58] Y. Zhang, T.T. Zuo, Z. Tang, M.C. Gao, K.A. Dahmen, P.K. Liaw, Z.P. Lu, Microstructures and properties of high-entropy alloys, Prog. Mater. Sci. 61 (2014) 1–93, https://doi.org/10.1016/j.pmatsci.2013.10.001.
- [59] C. Heremans, B.J. Wuensch, J.K. Stalick, E. Prince, Fast-ion conducting Y₂(Zr_yTi_{1-y})₂O₇ pyrochlores: neutron Rietveld analysis of disorder induced by Zr substitution, J. Solid State Chem. 117 (1995) 108–121, https://doi.org/10.1006/jssc.1995.1253.
- [60] A.F. Fuentes, S.M. Montemayor, M. Maczka, M. Lang, R.C. Ewing, U. Amador, A critical review of existing criteria for the prediction of pyrochlore formation and stability, Inorg. Chem. 57 (2018) 12093–12105, https://doi.org/10.1021/ ACS_INORGCHEM.8B01665.
- [61] E. Reynolds, P.E.R. Blanchard, Q. Zhou, B.J. Kennedy, Z. Zhang, L.Y. Jang, Structural and spectroscopic studies of La₂Ce₂O₇: disordered fluorite versus pyrochlore structure, Phys. Rev. B Condens. Matter 85 (2012) 1–5, https://doi.org/ 10.1103/PhysRevB.85.132101.
- [62] V. Kocevski, G. Pilania, B.P. Uberuaga, Modeling disorder in pyrochlores and other anion-deficient fluorite structural derivative oxides, Front. Chem. 9 (2021) 1–10, https://doi.org/10.3389/fchem.2021.712543.
- [63] C.L. Farrow, P. Juhas, J.W. Liu, D. Bryndin, E.S. Boin, J. Bloch, T. Proffen, S.J.L. Billinge, PDFfit2 and PDFgui: Computer programs for studying nanostructure in crystals, J. Phys. Condens. Matter 19 (2007), 335219, https://doi.org/10.1088/ 0953-8984/19/33/335219.
- [64] G. Pilania, B. Puchala, B.P. Uberuaga, Distortion-stabilized ordered structures in A2BB'07 mixed pyrochlores, Npj Comput. Mater. 5 (2019) 1–9, https://doi.org/ 10.1038/s41524-018-0144-1.
- [65] E.C. O'Quinn, K.E. Sickafus, R.C. Ewing, G. Baldinozzi, J.C. Neuefeind, M.G. Tucker, A.F. Fuentes, D. Drey, M.K. Lang, Predicting short-range order and correlated phenomena in disordered crystalline materials, Sci. Adv. 6 (2020), eabc2758, https://doi.org/10.1126/sciadv.abc2758.
- [66] D. Drey, E. O'Quinn, S. Finkeldei, J. Neuefeind, M. Lang, Local ordering in disordered Nd_xZr_{1-x}O_{2-0.5x} pyrochlore as observed using neutron total scattering, Acta Mater. 225 (2021), 117590, https://doi.org/10.1016/j.actamat.2021.117590.
- [67] F.P. Marlton, Z. Zhang, Y. Zhang, T.E. Proffen, C.D. Ling, B.J. Kennedy, Lattice disorder and oxygen migration pathways in pyrochlore and defect-fluorite oxides, Chem. Mater. 33 (2021) 1407–1415, https://doi.org/10.1021/ ACS.CHEMMATER.0C04515.
- [68] S. Il Kim, K.H. Lee, H.A. Mun, H.S. Kim, S.W. Hwang, J.W. Roh, D.J. Yang, W.H. Shin, X.S. Li, Y.H. Lee, G.J. Snyder, S.W. Kim, Dense dislocation arrays embedded in grain boundaries for high-performance bulk thermoelectrics, 348, Science 80 (2015) 109–114, https://doi.org/10.1126/science.aaa4166.



Dawei Zhang is currently a Ph.D. student at University of California, San Diego. His research focuses on the synthesis and characterization of high-entropy oxide materials for energy applications, e.g., thermal barrier coatings and thermochemical water splitting. He received a Master's degree in Material Science and Engineering from Stanford University in 2018.



Jian Luo graduated from Tsinghua University with dual Bachelor's degrees: one in Materials Science and Engineering and another in Electronics and Computer Technology, After receiving his M.S. and Ph.D. degrees from M.I.T., Luo worked in the industry for more than two years with Lucent Technologies Bell Laboratories and OFS/Fitel. In 2003, he joined the Clemson faculty, where he served as an Assistant/Associate/Full Professor of Materials Science and Engineering, In 2013, he moved to University of California, San Diego as a Professor of Nano-Engineering and Professor of Materials Science and Engineering. Luo group's current research focuses on interfaces in metals and ceramics, high-entropy and compositionally complex ceramics, ultrafast sintering and other novel ceramic processing technologies, high-temperature nanocrystalline alloys, and advanced materials for batteries and other energy-related applications. Luo received a National Science Foundation CAREER award in 2005 (from the Ceramics program) and an AFOSR Young Investigator award in 2007 (from the Metallic Materials program). He was a Vannevar Bush Faculty Fellow (2014) and a Minerals, Metals & Materials Society (TMS) Brimacombe Medalist (2019). Luo is a Fellow of the American Ceramic Society (2016), a Fellow of the ASM International (2022), and an Academician of the World Academy of Ceramics